The 2004 Las Campanas/Lowell Observatory Itokawa campaign:
I. Simultaneous visible and near-infrared photometry
of the Hayabusa mission target[*]

J. E. Thomas-Osip[1], S. M. Lederer[2,3], D. J. Osip[1], F. Vilas[3,4], D. Domingue[5], K. Jarvis[6], and S. L. Leeds[2]

[1]*The Observatories of the Carnegie Institute of Washington, Las Campanas Observatory, Colina El Pino, Casilla 601, La Serena, Chile*
[2]*California State University San Bernardino*
[3]*NASA/Johnson Space Center*
[4]*MMT Observatory*
[5]*Johns Hopkins University/Applied Physics Laboratory*
[6]*ESC Group/Hamilton Sundstrand*

In 2004, Asteroid 25143 Itokawa made its final close approach to the Earth prior to its encounter with the Japanese spacecraft Hayabusa. This apparition was superb with Itokawa reaching magnitude 12 (two magnitudes brighter than the 2001 apparition and the brightest since its discovery in 1998) and covering a large range of observable solar phase angles. An extensive visible and near-infrared observing campaign of Itokawa was undertaken at Las Campanas and Lowell Observatories to obtain full rotational coverage and cover the largest possible range of solar phase angles (4–129°). Unresolved global color mapping over the complete light curve (best fit synodic period of 12.118 hr) shows no sign of rotational color variability with upper limits of a few percent across the full U-thru-K spectrum. These combined multi-wavelength (UBVRIJHK) rotational light curves allow for the concrete deconvolution of shape from albedo variation in the rotational models and as required for Hapke modeling presented in Paper II (Lederer *et al.*, this issue), permits the removal of the rotational light curve effects from the solar phase curve. Furthermore, these derived solar phase curves can be fit with the IAU H,G magnitude system (Bowell *et al.*, 1989) thus allowing the calculation of geometric albedos ($p_v = 0.23 \pm 0.02$) as well as an estimate of the asteroid's elongated shape ($a/b = 1.9 \pm 0.1$) via the amplitude-phase relationtionship (Zappalà *et al.*, 1990). Results derived from the extensive ground-based campaigns are compared and contrasted with the much higher spatial resolution in situ measurements made by the Hayabusa spacecraft. The 'ground-truth' provided by the Hayabusa mission results shed light on the inferences that can begin to be made for the general asteroid population.
Key words: Asteroid Itokawa, near-Earth objects, spectrophotometry.

1. Introduction

The first sample return of an asteroid is planned in 2010. In September 2005, the Japanese spacecraft, Hayabusa, arrived at its near-Earth asteroid target, Itokawa, where it hovered above the surface of the asteroid until early December 2005. A major goal of this spacecraft mission was to touchdown twice on its surface to collect samples of the asteroid and bring them back to the Earth. Until the spacecraft returns, it will remain unknown whether samples were successfully collected. In the meantime, it is important to put what we have learned about Itokawa from Hayabusa in context with ground-based studies. Given the limitations inherent in ground-based observations, and the fact that this method will continue to be the most common way to learn about asteroids, we are most interested in qualifying the

type of ground-based studies best suited to physically characterize a more general population of asteroids in light of the 'ground-truth' provided by spacecraft in-situ investigations of a necessarily small sample of targets. By comparing and contrasting our extensive ground based results with the in situ measurements made by the Hayabusa spacecraft, we explore the implications for extending Hayabusa mission results to the general asteroid population.

Itokawa's 2004 closest approach provided the first opportunity since the asteroid was selected as the target for the Hayabusa mission to gather data on the asteroid at such a large range of solar phase angles (the Sun-asteroid-Earth angle). It was also the brightest apparition visible from the Earth since its discovery. Thus, we completed an extensive campaign of simultaneous visible and near infrared photometry (UBVRIJHK) in order to study rotational variability, rotational color variability, eight-color spectrophotometry, and solar phase angle effects. Section 2 describes the observational campaign in detail including descriptions of the instruments and telescopes used and the full data set collected. Section 3 discusses data reduction. In Sec-

---

Table 1. Observing details.

Solar Phase Angle[a]	Filters	Dates (2004)	r (AU)[a]	Δ (AU)[a]	# of nights	Telescope
4°	BVRI	Jan 26	1.32	0.34	1	Baade 6.5-m
11°	UBVRIJHK	Jul 29–30	1.13–1.14	0.12–0.13	2	Swope 1-m, duPont 2.5-m
4°–19°	BVRI	Jan 24–Feb 9	1.02–1.33	0.30–0.35	8	Perkins 1.7-m
19°–25°	UBVRI	Jul 13–17	1.07–1.09	0.06–0.07	3	Swope 1-m
32°–50°	UBVRIJHK	Jul 2–8	1.03–1.05	0.02–0.04	6	Swope 1-m, duPont 2.5-m
53°–70°	UBVRI	Jun 29–Jul 1	1.02–1.03	0.01–0.02	3	Swope 1-m
129°	BVRI	Jun 6	0.97	0.08	1	Clay 6.5-m

[a]Giorgini *et al.* (1996).

tions 4, 5, and 6, the analysis of the rotational light curves, solar phase curves, and eight-color spectrophotometry are presented, respectively. Further analysis of the solar phase curve to look more in-depth at the surface properties is presented in a second paper Lederer *et al.* (this issue), hereafter Paper II.

2. Observational Campaign

An extensive visible and near-infrared observing campaign of Itokawa was undertaken at Las Campanas Observatory (LCO) in Chile and Lowell Observatory in Arizona. This apparition was superb with Itokawa reaching magnitude 12 (two magnitudes brighter than the 2001 apparition) and covering a large range of observable solar phase angles. Ideal placement in the southern hemisphere in June and July 2004 yielded 14 nights of UBVRI photometric observations with simultaneous JHK observations on 8 of those nights at LCO. The entire rotational period and solar phase angles between 11–90 degrees were sampled. Additionally, we obtained 8 nights of BVRI broadband photometry data in January and February 2004 at Lowell Observatory as well as BVRI observations with the Magellan 6.5 meter telescopes in both January and June. These data extend the solar phase angle coverage for the BVRI filters to a range from 4° out to 129°.

This campaign was designed to maximize both rotational angle and solar phase angle angle coverage. With two blocks of simultaneous near-infrared (using the duPont 2.5 m) and visible (using the Swope 1.0 m) observations separated by 20 days we were able to observe Itokawa over a complete rotational period (the observable rotational longitudes change slowly from day to day as the rotational period is just over 12 hours and nearly commensurate with a multiple of the Earth day) across the full wavelength range U–K. Furthermore, with additional observations made with the Swope, Magellan, and Perkins telescopes we were able expand the phase angle coverage and dramatically improve the physical characterization of the body and its surface. Table 1 summarizes the observing details, including the observing dates, the heliocentric (r) and geocentric (Δ) distances of the asteroid, the solar phase angle (α), the filters employed on that date, and the observatory.

2.1 Telescope/Instrument descriptions

Due to simultaneous access to the Swope and duPont telescopes as well as additional access to the Magellan telescopes at LCO and the Perkins telescope at Lowell by the same observers, we were able to achieve high consistency in data quality.

Table 2. Filter effective wavelengths and solar colors.

Filter	Effective Wavelength (μ)	Solar Color (V^a- Filter)
U	0.36	−0.84[b]
B	0.44	−0.67[c]
V	0.54	0
R	0.63	0.37[c]
I	0.8	0.71[c]
J	1.25	1.08[d]
H	1.65	1.41[d]
K	2.16	1.45[d]

[a]$V = -26.74$[c], [b]Lang (1992), [c]Howell (1995), [d]Tokunaga (2001).

2.1.1 Las Campanas Observatory The majority of the visible observations at LCO were made using the Swope 1 meter telescope (Bowen and Vaughan, 1973) and the Direct CCD Camera with a SITe detector. This combination has a field of view of $14.8' \times 22.8'$ and an image scale of $0.435''$/pixel. Additionally, for the purpose of efficiency, most frames were taken in a sub-raster mode resulting in a field of view of $8.7' \times 8.7'$. A UBVRI filter set was used that contains Harris BVR filters, a Washington T2 (I in the Krons-Cousins system) filter, and a Johnson U filter (see Table 2 for the effective wavelengths of these filters). For the purpose of these observations this telescope was upgraded to move at non-sidereal tracking rates. Due to the large variation in the rates of motion of Itokawa during the observing run and the learning curve on the non-sidereal rates control system, the tracking rates used by the telescope were not always perfect and some trailing (mostly in the longer U exposures) occurred.

Additional visible observations were obtained employing the MagIC and IMACS instruments on the two Magellan 6.5 meter telescopes. Our earliest data were obtained at LCO in January of 2004 when multiple sets of BVRI images were collected with the direct CCD camera MagIC (Osip *et al.*, 2004) on the Clay telescope. The highest phase angle data were obtained from LCO in June of 2004 when BVRI imaging was carried out from the multi-object spectrograph and imager, IMACS (Dressler *et al.*, 2006).

The near-IR observations were made using the duPont 2.5 meter telescope (Bowen and Vaughan, 1973) and the Wide-Field Infrared Camera (WIRC). WIRC (Persson *et al.*, 2002) has four 1024×1024 Rockwell HgCdTe detectors, however, for the purpose of efficiency only one of these was used for this project. This combination has a field of view of $3.35'$ square and a image scale of $0.196''$/pixel. The JHK filter set used contains Carnegie J_c and H_c filters along with a K_s filter designed to reduce thermal background at

ground based sites (Persson *et al.*, 1998, 2002). At the time of the NIR observations, Itokawa was bright and moving rapidly (1–17″/min; Giorgini *et al.*, 1996). Thus, exposure times were short, ranging from 3–10 seconds. Dithering for the asteroid frames was provided by maintaining sidereal telescope tracking rates and simply allowing normal asteroid motion over sets of 10–15 frames depending on the filter choice. Standard stars were observed using a dice-5 dither pattern.

2.1.2 Lowell Observatory Data from Lowell Observatory were obtained with the 72″ (1.8 m) Perkins Telescope and the 2048×2048 Loral charge-coupled device (CCD) camera (2×2 binned). The image scale for this system is 0.191″/pixel and the field of view 3.26′ square. Johnson broadband BVRI filters were employed for this run; the asteroid was too faint to obtain U-band observations during this time. The observations of the asteroid were taken while tracking at the asteroid's predicted ephemeris rate.

3. Data Reduction

Due to the different methods of data collection in the visible and near-infrared slightly different processes were used to reduce these different data sets. Generally, however, all images were bias and dark corrected and flattened; instrumental magnitudes were converted to apparent magnitudes in the UBVRIJHK system through the use of Landolt or Persson faint IR standards. Furthermore, reduced magnitudes (the magnitude the asteroid would have if it were located at the standard, but physically nonexistent, location of 0° solar phase angle and 1 AU from both the Sun and the Earth) were then calculated from the following:

$$m_r = m_a - 5\log(\Delta r) \qquad (1)$$

where m_a is the observed apparent magnitude, Δ is the distance between the Earth and the asteroid, and r is the asteroid's heliocentric distance.

3.1 Visible photometry

The visible band data taken both at Lowell Observatory (1.8 m Perkins telescope) and at Las Campanas Observatory (1.0 m Swope telescope) were reduced in the same manner, employing the IRAF (Image Reduction and Analysis Facility) software for all data reduction (Tody, 1986, 1993). All data included in the analysis were taken under photometric conditions. Twilight-sky exposures were used to generate the master flat field for each filter on each run. After initial bias subtracting and flat fielding, all other instrumental artifacts such as cosmic rays and bad rows/columns were removed in the standard manner. The IRAF PHOT package in DAOPHOT was used to extract photometry of the standard stars and the asteroid. PHOT calculates the photometry within a circular aperture, and subtracts the sky median average within an annulus around the circular aperture. To improve the signal-to-noise ratio, the smallest possible aperture was chosen that included the full signal from the target object. Aperture sizes chosen for a given night, therefore, varied depending upon the seeing conditions (and minor trailing in the case of long U band images). All observations with background star contaminations were eliminated from further analysis. Although a small effect due to Itokawa's proximity to Earth, observations were corrected

for light-travel time. Landolt standard star observations, covering a full range of colors and airmasses, were taken during the observing run and used to absolutely calibrate the observations (Landolt, 1992). The observations at Magellan were reduced in a similar fashion, via bias subtraction and flat fielding of all target and standard star frames followed by circular aperture photometry of all targets using IDL routines equivalent to the IRAF DAOphot packages.

3.2 Near-Infrared photometry

The near-infrared frames selected to be taken during photometric conditions were flat fielded using flats created by subtracting a lamp-off, median filter combined flat field from the lamp-on, median filter combined flat field. This subtraction of the lamp-off flat is necessary, especially at the K-band, in order to remove thermal emission background effects from the surrounding dome. This method also removes any bias levels. A separate dark current subtraction was made using dark frames with exposure times equal to those in the science images. Circular aperture photometry was performed on the flattened images using the aper routine from the GSFC's astronomy user's library of IDL routines (Landsman, 1993). A curve of growth was used to account for variable seeing and keep the signal-to-noise ratio roughly constant. Sky subtraction was performed by combining each set of dither patterns into a sky image that was then subtracted from the science images before the aperture photometry was performed. For standard stars a dice-5 dither pattern was used to create the sky frames. With sidereal tracking and a fast-moving asteroid, each set of 10–15 asteroid images provided enough dithering to make corresponding sky frames. IDL scripts were developed by the authors to handle the WIRC data using the IDL astronomy user's library IDLPHOT aperture photometry package (Landsman, 1993). Calibration from instrumental magnitudes to standard magnitudes was performed through the observation of faint IR standards (Persson *et al.*, 1998).

4. Rotational Light Curves

The observations, once converted to reduced magnitudes, were plotted as a function of rotational phase angle. All data were phased rotationally by arbitrarily assuming 0° rotational phase angle to have occurred at the beginning of the julian day of the first NIR observation ($JD_{ref} = 2453188$) and a best fit synodic period of 12.118±0.001 hours. Thus the rotational phase angle in radians is given by:

$$\omega = 2\pi \,\mathrm{mod}[24(JD_{obs} - JD_{ref}), 12.118] \qquad (2)$$

Solving for the pole position and developing a shape model for Itokawa indicate a sidereal period as found by Kaasalainen *et al.* (2003, 12.132±0.0005). A subset of the highest time resolution data from the present study was analyzed by Kaasalainen (p.c.) verifying a perfect fit to the adopted shape model and pole position. In this study however, the synodic light curve period chosen is the period that best allows the lightcurves from different days to be phased together to form the rotational light curves. To examine the rotational light curve properties, the brightness variations due to solar phase angle variations need to be removed from the data set. A first order removal of the solar phase
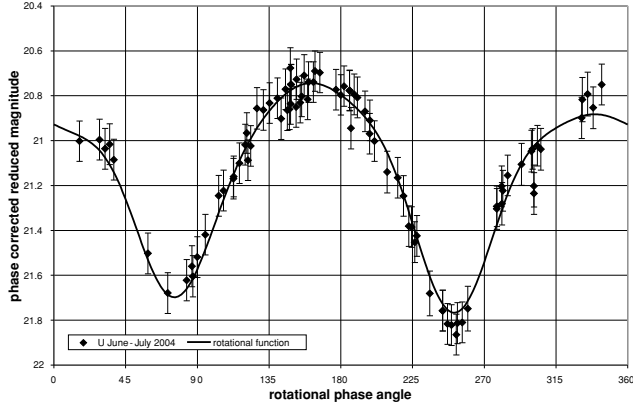
Fig. 1. Points indicate the observed rotational light curve in the U filter during June–July 2004 where the reduced magnitudes have been corrected for an empirical phase variation according to Eq. (3). The line shows the function fit to the observed light curve via Eq. (A.2).
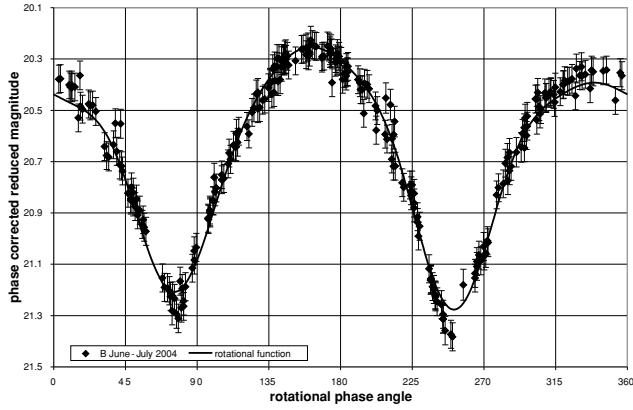

Fig. 3. Points indicate the observed rotational light curve in the V filter during June–July 2004 where the reduced magnitudes have been corrected for an empirical phase variation according to Eq. (3). The line shows the function fit to the observed light curve via Eq. (A.2).

Fig. 2. Points indicate the observed rotational light curve in the B filter during June–July 2004 where the reduced magnitudes have been corrected for an empirical phase variation according to Eq. (3). The line shows the function fit to the observed light curve via Eq. (A.2).

Fig. 4. Points indicate the observed rotational light curve in the R filter during June–July 2004 where the reduced magnitudes have been corrected for an empirical phase variation according to Eq. (3). The line shows the function fit to the observed light curve via Eq. (A.2).

variations was performed by using the following empirical relationship:

$$m_{\mathrm{solar}} = m_r - 0.028\alpha \qquad (3)$$

where m_{solar} is the reduced magnitude empirically corrected for solar phase angle variations and α is the solar phase angle in degrees. Figures 1 through 8 show the resulting rotational light curves for each filter with the solar phase variations empirically removed for the June/July 2004 time period. Figures 9 through 12 show the same but for the January/February 2004 time period. Both the June/July 2004 and Jan/Feb 2004 timeframes covered a full rotation period allowing us to fit a functional rotational light curve to the observations in Section 4.2.

4.1 Rotational color properties

Colors were calculated by linearly interpolating the J filter observations (made with the highest temporal frequency) to find the J magnitudes at the times the other filter observations were made. Points were carefully selected such that no interpolations were made over light curve minima or maxima. Figures 13 and 14 show the colors, U-B, V-B, V-R, R-I, V-J, J-H, and J-K as a function of rotational phase angle for observations made July 2, 3, 4, 5, 8, 30,
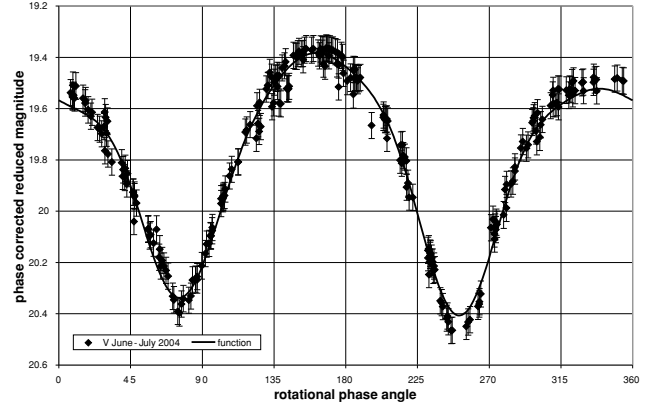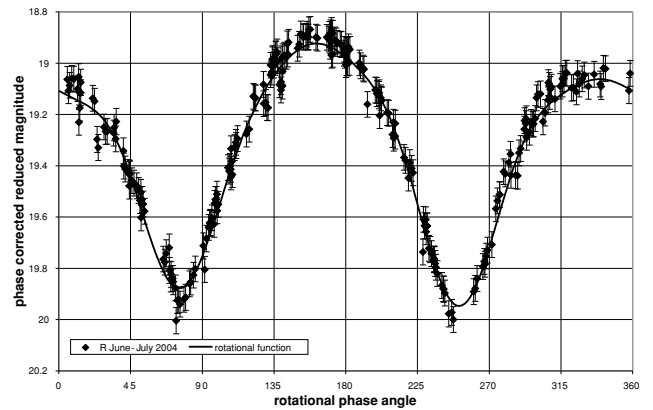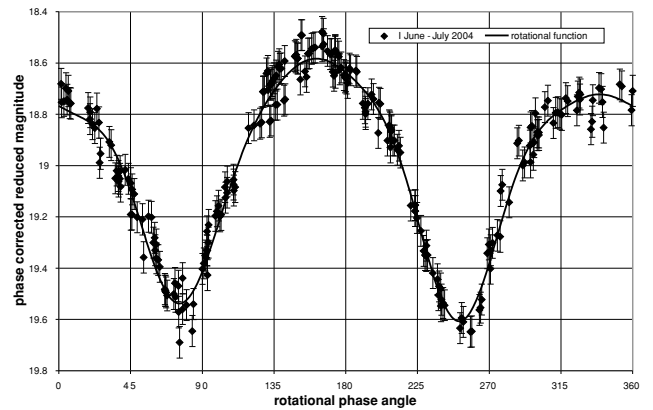

Fig. 5. Points indicate the observed rotational light curve in the I filter during June–July 2004 where the reduced magnitudes have been corrected for an empirical phase variation according to Eq. (3). The line shows the function fit to the observed light curve via Eq. (A.2).

31 when all eight filters were used. The solar colors in Table 2 were subtracted. Any rotational color variability is found to be well within the average uncertainties. This is in contrast to the rotational color variation seen by Lowry *et*
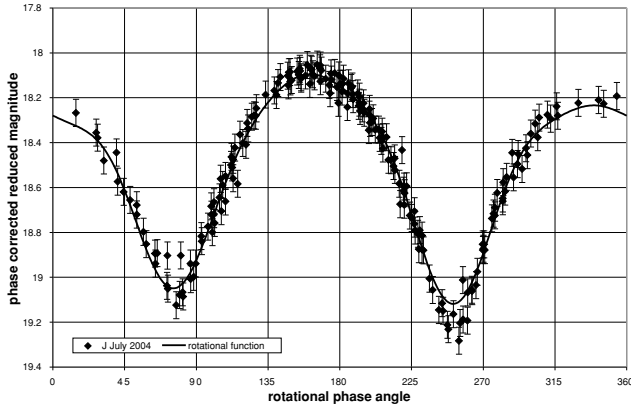
Fig. 6. Points indicate the observed rotational light curve in the J filter during June–July 2004 where the reduced magnitudes have been corrected for an empirical phase variation according to Eq. (3). The line shows the function fit to the observed light curve via Eq. (A.2).
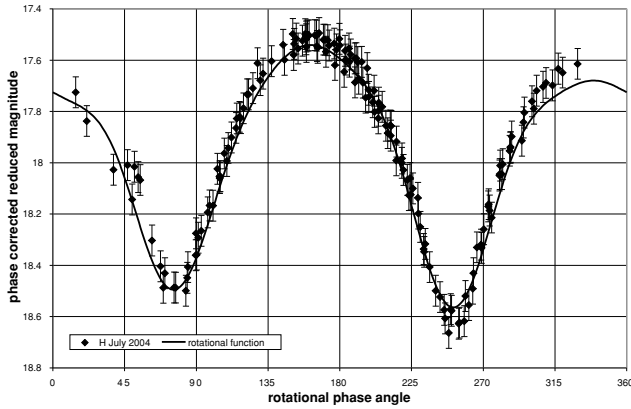

Fig. 9. Points indicate observed rotational light curve in the B filter during Jan/Feb 2004 where the reduced magnitudes have been corrected for an empirical phase variation according to Eq. (3). The line shows the function fit to observed light curve via Eq. (A.1).

Fig. 7. Points indicate the observed rotational light curve in the H filter during June–July 2004 where the reduced magnitudes have been corrected for an empirical phase variation according to Eq. (3). The line shows the function fit to the observed light curve via Eq. (A.2).
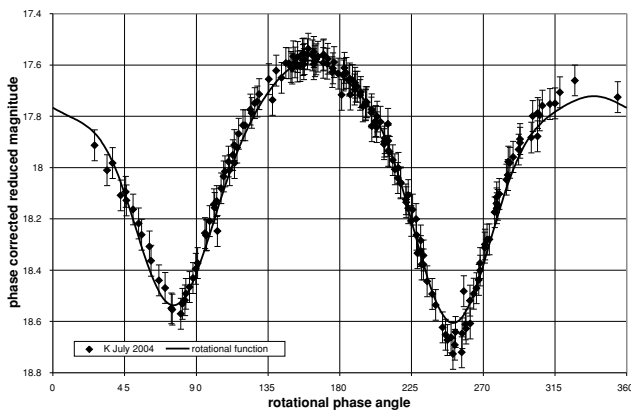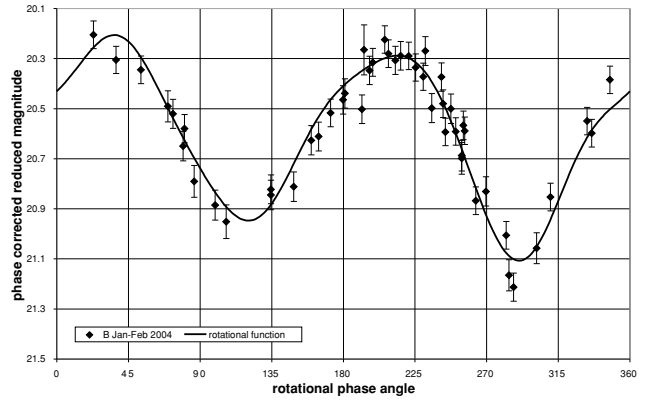

Fig. 10. Points indicate observed rotational light curve in the V filter during Jan/Feb 2004 where the reduced magnitudes have been corrected for an empirical phase variation according to Eq. (3). The line shows the function fit to observed light curve via Eq. (A.1).

Fig. 8. Points indicate the observed rotational light curve in the K filter during June–July 2004 where the reduced magnitudes have been corrected for an empirical phase variation according to Eq. (3). The line shows the function fit to the observed light curve via Eq. (A.2).

Fig. 11. Points indicate observed rotational light curve in the R filter during Jan/Feb 2004 where the reduced magnitudes have been corrected for an empirical phase variation according to Eq. (3). The line shows the function fit to observed light curve via Eq. (A.1).
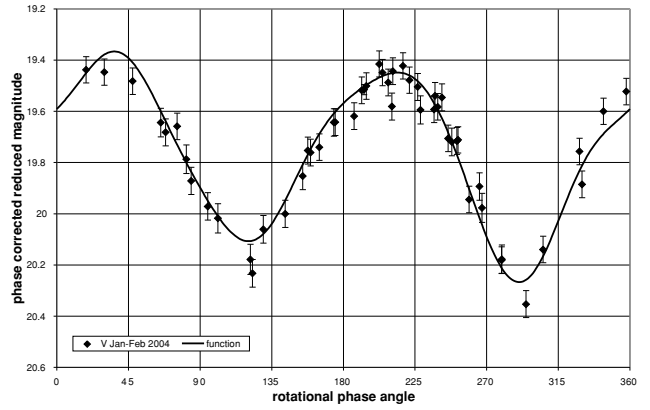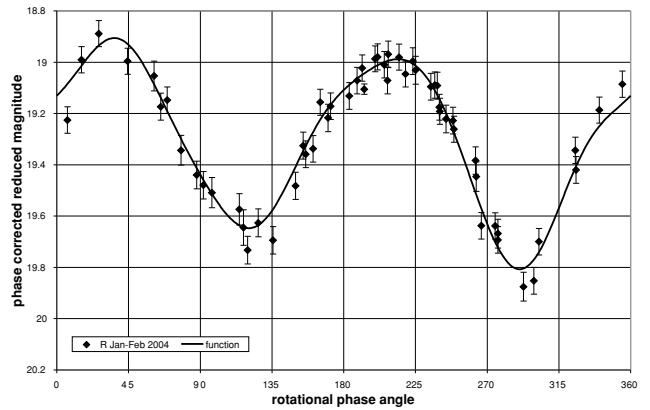
al. (2005) where incomplete sampling of the full rotational period may have introduced more uncertainties than previously accepted. The color variations seen by Hayabusa spacecraft (Saito *et al.*, 2006) occur at far too fine a spa-

tial resolution to be detected in ground-based unresolved global mapping. The average colors were also determined and are displayed in the third column of Table 4 and discussed futher in Section 6.1.
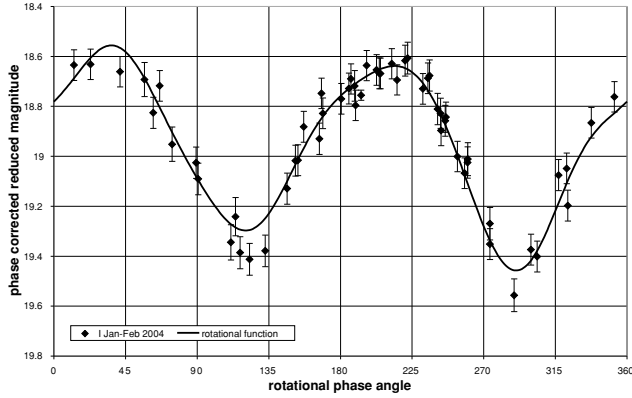
Fig. 12. Points indicate observed rotational light curve in the I filter during Jan/Feb 2004 where the reduced magnitudes have been corrected for an empirical phase variation according to Eq. (3). The line shows the function fit to observed light curve via Eq. (A.1).

4.2   Rotational light curve modeling

The lack of rotational color variation seen in the U through K broadband filters, as demonstrated in Figs. 13 and 14, suggests that the observed rotational variations are due to changes in the visible projected area of an irregularly shaped body and not variation in albedo. Therefore, the rotational properties can be modeled by fitting an empirical function to the rotational light curves over limited periods of time. The functions applied to model the rotational light curve behavior use linear combinations of sine and cosine functions. The functions have the form:

$$m_r = C + F(\omega) \qquad (4)$$

where m_r is the observation in reduced magnitudes, C is a constant equal to the average of reduced magnitude over rotation angle, ω is the rotational phase angle (in radians), and $F(\omega)$ is a linear combination of sine, cosine, and their multiples with ω as the argument. Separate functions were used for the data obtained during the time periods of January through February 2004, and June through July 2004, respectively (the functions are provided in Appendix A). The fits of these functions to the observational data were performed using a standard linear regression technique in *Mathematica^{TM}*. Figures 1 through 12 show the functions describing the rotational light curves in comparison to the observed light curves.

4.2.1   Removal of rotational light curve effects in the solar phase curve

In order to model the brightness variations as a function of solar phase angle the rotational light curve variations must first be removed from the observational data set. The rotationally corrected reduced magnitude, m_{rr} was obtained using the following relationship:

$$m_{rr} = m_r - F(\omega) \qquad (5)$$

where $F(\omega)$ is defined in Eq. (4). The resulting rotationally corrected reduced magnitudes were converted to absolute magnitudes, m_a, using the relationship

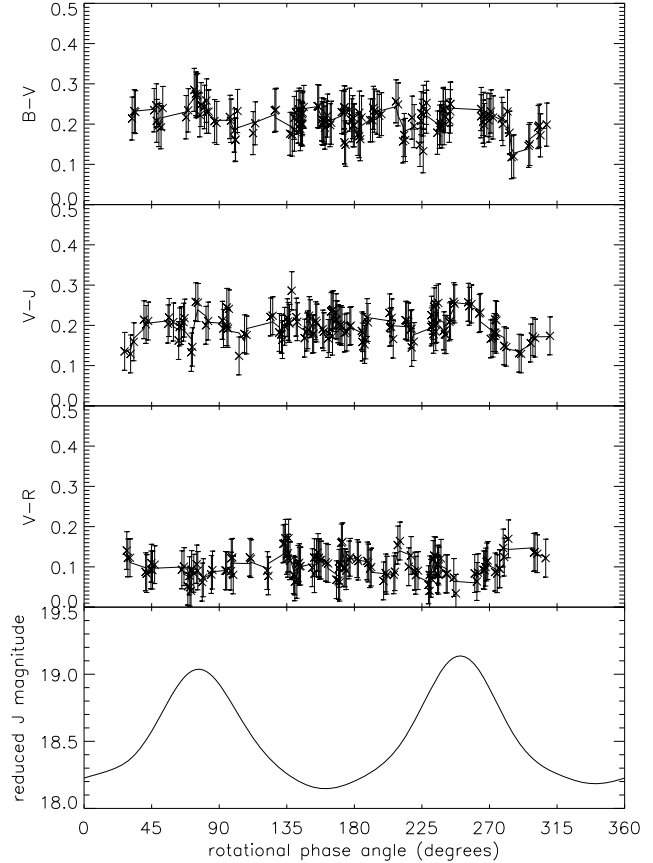$$m_a = m_{rr} - m_s - 2.5 \log\left(\frac{\pi}{A}\right) + \log s \qquad (6)$$

Fig. 13. Colors B-V, V-J, and V-R as a function of rotational phase angle for observations made July 2, 3, 4, 5, 8, 30, 31 when all eight filters were used. The solid line in the top three panels shows a box-car average of width nine. Bottom panel shows the modeled J light curve (note compressed magnitude scale) for comparison purposes.

where A is the projected area of the asteroid, s is the Earth-Sun distance at the time of observation, and m_s is the magnitude of the sun as seen from distance s. Table 2 lists the solar magnitudes for the broadband filters used in this study. The value of A was assumed to be the average projected area for an ellipsoid with the dimensions 548-m by 312-m by 276-m; the dimensions of Itokawa as estimated from radar observations (Ostro *et al.*, 2004). Based on estimates of the latitude of the rotational pole ($-89° \pm 5°$ by Kaasalainen *et al.*, 2003), the assumption was made that this set of Earth-based observations had sub-observer points near the equator. Therefore the average visible projected area was calculated assuming an equatorial sub-observer point. Figure 15 shows an example of the solar phase curves produced by removal of the rotational effects in comparison to the uncorrected. The corrections above produce the solar phase curves shown in Fig. 16.

5.   Solar Phase Curves

The solar phase curves in Fig. 16 were fit via IAU adopted H-G magnitude system (Bowell *et al.*, 1989) where H is termed the absolute magnitude (defined at the rotational light curve mid-point) and G is a slope parameter. These fits are also shown in Fig. 16. Table 3 shows the H-G parameters for all eight filters. Notably, the estimate of the absolute magnitude in the V band is refined
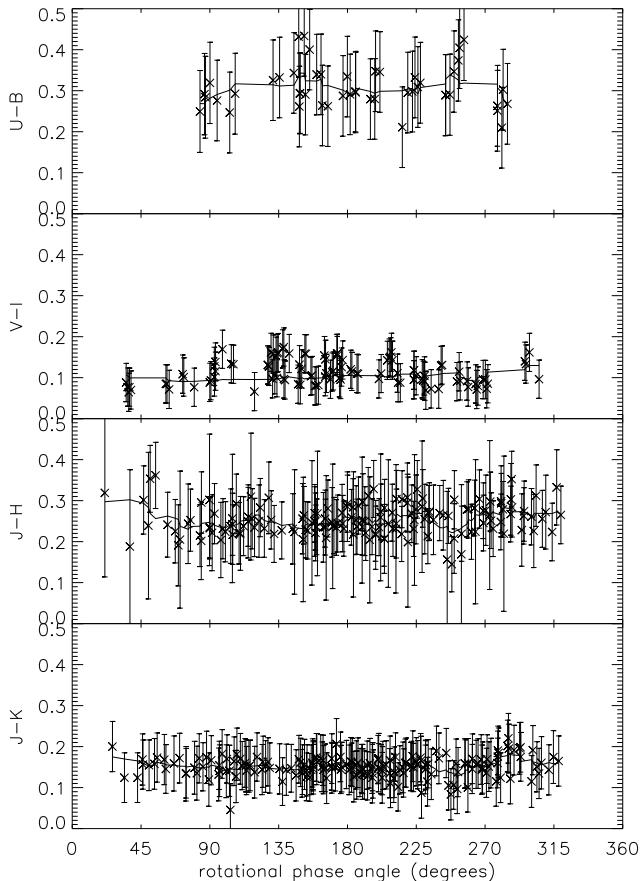
Fig. 14. Colors U-B, V-I, J-H, and J-K as a function of rotational phase angle for observations made July 2, 3, 4, 5, 8, 30, 31 when all eight filters were used. The solid line shows a box-car average of width nine.
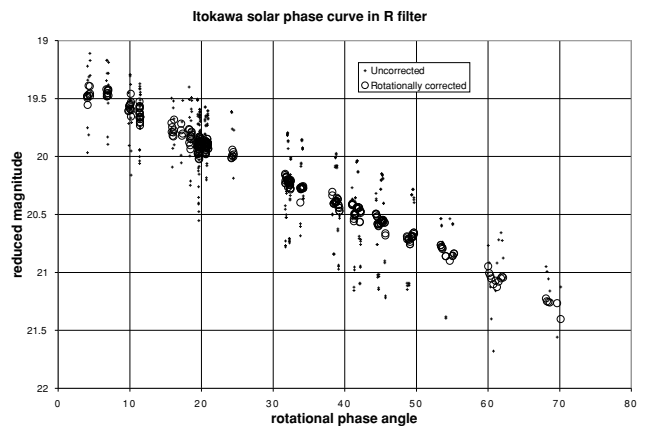

Fig. 15. Example of solar phase curve with and without rotational correction for the R filter.
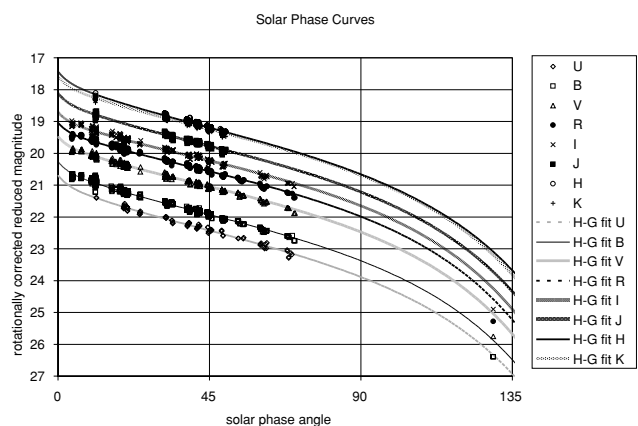
Fig. 16. Solar phase curves in all eight filters and their respective fits in the H, G magnitude system.

to be 19.472 ± 0.006 as compared with a previous estimate of 19.73 ± 0.17 (Abe *et al.*, 2002). Using the following relationship between object radius (r), H, the apparent magnitude of the Sun ($M_\odot$) and geometric albedo (p) (c.f Tomasko, 1976, p. 490):

$$\log p = 0.4(M_\odot - H) - 2 \log r + 16.35 \qquad (7)$$

we can give a very good estimate for the geometric albedo. We use the radius of a sphere of equal surface area (0.393 km^2) as measured by the Hayabusa spacecraft (Demura *et al.*, 2006). Thus, we find a visual albedo of 0.23 ± 0.02, which is consistent with that reported by Müller *et al.* (2005) but with significantly smaller uncertainty. This is completely consistent with an average S class asteroid and significantly lower than that determined in the 2001 apparition (Abe *et al.*, 2002; Dermawan *et al.*, 2002; Lederer *et al.*, 2005) most likely because of the more limited range of solar phase angles available in 2001. Furthermore, the phase integral and bond albedo can also be estimated following Bowell *et al.* (1989). Table 3 also includes geometric albedos (p), phase integrals (q), and bond albedos (A) calculated for all eight filters. Further analysis of the phase curve and inference of surface properties through the use of Hapke modeling is provided in Paper II. It is important to note that although the geometric albedos agree to within their errors, the phase integrals and bond albedos in Table 3 are significantly different than those in Table 9 of Paper II.

This illustrates an important difference between the *H-G* magnitude system, based on the Lumme and Bowell photometric model, and the Hapke photometric model.

5.1 Amplitude/Solar phase angle correlations

To examine the correlation between the amplitude of the rotational light curve and the solar phase angle (Zappalà *et al.*, 1990), an amplitude was determined for each individual light curve (per night) for which there were enough points to clearly determine a maximum and a minimum. Amplitudes for phase angles less than $40°$ in all filters were least squares fit with a line to find the amplitude at zero phase angle, $A(0°)$ and the slope, s(APR). Amplitude variation with phase angle is primarily due to geometrical effects (Gutiérrez *et al.*, 2006). It is therefore, unnecessary, to fit each filter separately. All filters were combined together to increase the number of points to fit. The maximum number that came from any one filter was seven. We find $A(0°) = 0.69 \pm 0.02$ magnitudes and s(APR)=0.010 ± 0.001 magnitudes per degree.

Given that Itokawa's pole position is practically perpendicular to the ecliptic plane (Demura *et al.*, 2006), it is a reasonable assumption that throughout this apparition both the aspect and obliquity angles were almost constant (and near $90°$). If we then assume that the rotational variability is due solely to shape as we did above in correcting the so-

Table 3. *H* and *G* parameters and the resulting geometric albedos (p), phase integrals (q) and bond albedos (A).

Filter	H	H error	G	G error	p	p error	q	q error	A	A error
U	20.688	0.018	0.141	0.008	0.167	0.017	0.386	0.005	0.065	0.102
B	20.26	0.006	0.176	0.004	0.21	0.021	0.41	0.003	0.086	0.1
V	19.472	0.006	0.228	0.004	0.234	0.023	0.446	0.003	0.104	0.1
R	19.038	0.006	0.253	0.004	0.248	0.025	0.463	0.003	0.115	0.1
I	18.707	0.008	0.256	0.005	0.246	0.025	0.465	0.003	0.114	0.101
J	18.114	0.016	0.181	0.008	0.302	0.031	0.414	0.005	0.125	0.102
H	17.428	0.022	0.127	0.01	0.42	0.043	0.377	0.007	0.158	0.104
K	17.591	0.015	0.182	0.008	0.348	0.035	0.414	0.005	0.144	0.102

lar phase curve for rotational effects, we can use the light curve amplitude at 0° solar phase angle to make an estimate of Itokawa's elongation (a/b, where a is the longest axis and b is the second longest axis) as in the following relation:

$$\log \frac{a}{b} = 0.4A(0°)$$ (8)

$$\sigma_{\frac{a}{b}} = \sigma_{A(0°)} 10^{0.4A(0°)} 0.4 \ln 10$$ (9)

This gives $a/b = 1.9 \pm 0.1$ which is in good agreement with $a/b = 1.820 \pm 0.007$ as calculated from the size of Itokawa measured by the Hayabusa spacecraft (Demura *et al.*, 2006).

6. Spectrophotometry

To examine normalized reflectance as a function of wavelength between U and K during July 2004, data points in all other filters were interpolated linearly to the time of the nearest U data point since this filter had the lowest time resolution. The reduced magnitudes were converted to flux and normalized to 1 at the I filter effective wavelength of 0.8μ. They were then divided by the solar flux also normalized to the I band found from the solar colors and magnitude shown in Table 2. The 35 sets of spectrophotometry with a maximum time between all eight filter measurements of less than 30 minutes were averaged to produce the spectrophotometry shown in Fig. 17. Spectra taken during the 2001 apparition by Abell *et al.* (2006) and Binzel *et al.* (2001) are shown for comparison. Both spectra appear to agree with our spectrophotometry to within our error bars. Further discussion of the differences between these spectra can be found in Abell *et al.* (2006).

6.1 Broadband characteristics

Table 4 shows our calculated average values for broadband colors U-B, B-V, V-R, R-I, V-I, V-J, J-H, and J-K. The values listed here are solar-corrected colors, defined as observed color of the asteroid minus the equivalent solar value as found in Table 2. The errors listed for the colors represent the 1-sigma standard deviation for the range of dates listed. In the case of the first two columns of Table 4, pairs of photometric data points were chosen carefully, limiting our choices to data taken sequentially in time where less than 10 minutes had passed between the two observations to prevent any color variations to be caused by rotational phase induced brightness variations. The values in the third column of Table 4 were determined as discussed in Section 4.1. Our visible colors agree to within the errors listed with those reported by Lowry *et al.* (2005, note that the asteroid
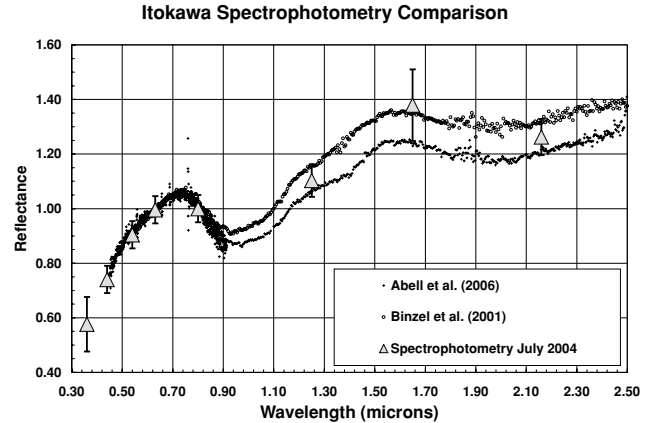

Fig. 17.   Spectrophotometry in comparison to spectra taken during the 2001 apparition by Abell *et al.* (2006) and Binzel *et al.* (2001).

Table 4.   UVBRIJHK broadband colors.

Color	Jan/Feb 2004	Jun/Jul 2004	Jul 2004
U-B	–	0.32 ± 0.15	0.31 ± 0.06
B-V	0.18 ± 0.09	0.20 ± 0.10	0.21 ± 0.04
V-R	0.09 ± 0.07	0.09 ± 0.07	0.10 ± 0.04
R-I	0.03 ± 0.08	0.01 ± 0.11	0.01 ± 0.06
V-I	0.12 ± 0.11	0.10 ± 0.09	0.11 ± 0.04
V-J	–	–	0.19 ± 0.03
J-H	–	–	0.25 ± 0.04
J-K	–	–	0.15 ± 0.02

colors listed by Lowry are not solar-corrected). Furthermore, our near-infrared color J-K agrees with that reported by Ishiguro *et al.* (2003, again noting that their values are not solar-corrected), however, our J-H value is about 15% higher than found previously. Regardless of this difference, the near infrared colors are still completely consistent with those of an S-class asteroid (Sykes *et al.*, 2000). This appears to be the first V-J color reported for Itokawa.

Broadband colors suggest that Itokawa is indeed an S-class asteroid, but somewhat of an outlier when compared with the main-belt S-class asteroids. Itokawa is slightly redder in color. A small S-class asteroid like this one is generally expected to be less altered, and thereby less reddened than the larger asteroids. Itokawa, however, follows the color characteristics typically seen in a larger, "space-weathered" S-class asteroid.

7.   Conclusions and Recommendations

The physical characterization of asteroid Itokawa derived from our uniform multi-wavelength ground-based observations are very consistent with results from other ground-based campaigns as well as with the "ground-truth" found from in situ measurements by the Hayabusa spacecraft. Global colors across the U-K spectrum are redder than solar and are most consistent with an S-type classification. Fine scale albedo and color variation seen by Hayabusa spacecraft (Saito *et al.*, 2006) occur at too high a spatial resolution to be detected in any ground-based light curves. The combined multi-wavelength (UBVRIJHK) rotational light curves show no measurable sign of rotational color variability and are best fit by a synodic rotation period of 12.118±0.001 hours. This is consistent with the 12.132 hr sidereal period, pole position and rudimentary shape model of Kaasalinen 2003 as well as the more precise shape modeling from the Hayabusa imaging (Demura *et al.*, 2006). Attributing rotational variability to shape rather than albedo, simple modeling permits the removal of the rotational light curve effects from the solar phase curves. These solar phase curves are fit with the IAU H,G magnitude system (Bowell *et al.*, 1989) thus allowing the calculation of geometric albedos ($p_v = 0.23 \pm 0.02$) that are consistent with those found by Müller *et al.* (2005). Furthermore, using the amplitude-phase relationship (Zappalà *et al.*, 1990), we estimate an elongated shape ($a/b = 1.9 \pm 0.1$) entirely consistent with Hayabusa results (Demura *et al.*, 2006) estimating $a/b = 1.820 \pm 0.007$.

Detailed Hapke modeling is presented in Paper II indicating that Itokawa has a blocky surface whose regolith differs from other (albeit larger) S-type asteroids for which Hapke modeling has been performed to date. This indicates the need for further observations and Hapke modeling of asteroids over a wider size range and across taxonomic classes. While geometrical albedo estimates remain consistent between H-G system calculations and Hapke modeling, differences in the phase integrals and bond albedo estimates (c.f. Paper II) further enhance the need for additional detailed observations and physical light scattering modeling of a broader sample of asteroid surfaces.

In consideration for future spacecraft missions, we can make a few more recommendations for both the spacecraft planners and ground-based observers. It is important to define scientific targets well in advance to allow for multi-epoch campaigns prior to the mission. This allows for favorable viewing geometry and wider phase angle coverage from multiple observatories as well as providing for discrimination of target pole position and sense of rotation. In all cases, sufficient rotational and wavelength coverage will be required to remove rotational effects from the solar phase curves. The largest possible phase angle coverage is desired to constrain results of detailed light scattering modeling like the Hapke parameterization detailed in Paper II. Finally, adoption of a standardized high transmission filter suite (i.e. Sloan u′, g′, r′, i′, z′) by both ground-based observers and spacecraft would allow for higher throughput, improved color determinations, and better cross calibration.

Appendix A. Rotational Functions

January/February 2004 (including all Lowell points and the Magellan 4° solar phase angle point):

$$
\begin{aligned}
F(\omega) = \bar{M}_r - [& -0.011\cos\omega - 0.218\cos 2\omega \\
& -0.004\cos 3\omega + 0.027\cos 4\omega \\
& +0.026\cos 5\omega + 0.011\cos 6\omega \\
& -0.060\sin\omega - 0.295\sin 2\omega \\
& +0.029\sin 3\omega + 0.050\sin 4\omega \\
& -0.007\sin 5\omega + 0.006\sin 6\omega] \quad \text{(A.1)}
\end{aligned}
$$

June/July 2004 (including all Swope and duPont points and the Magellan 120° solar phase angle point):

$$
\begin{aligned}
F(\omega) = \bar{M}_r - [& 0.027\cos\omega - 0.357\cos 2\omega \\
& +0.044\cos 3\omega + 0.050\cos 4\omega \\
& -0.005\cos 5\omega + 0.010\cos 6\omega \\
& -0.024\sin\omega + 0.233\sin 2\omega \\
& -0.0284\sin 3\omega - 0.100\sin 4\omega \\
& +0.012\sin 5\omega + 0.029\sin 6\omega] \quad \text{(A.2)}
\end{aligned}
$$

References

Abe, M., Y. Ohba, M. Ishiguro, S. Hasegawa, T. Fuse, K. Aoki, Y. Ohyama, N. Kashikawa, FOCAS team, A. Tokunaga, M. Goto, T. Usuda, H. Terada, N. Kobayashi, IRCS team, and A. Fujiwara, Physical Model and Taxonomic Type of 1998 SF36, the Target Asteroid of Sample Return Mission, Muses-C, *Lunar and Planetary Science Confernce Series*, **33**, 1666–1667, 2002.

Abell, P., F. Vilas, K. S. Jarvis, M. J. Gaffey, and M. S. Kelley, Mineralogical Composition of (25143) Itokawa 1998 SF_{36} from visible and Near-Infrared Reflectance Spectroscopy: Evidence for Partial Melting, *Meteoritics and Planetary Sciences*, 2006 (submitted).

Binzel, R. P., A. S. Rivkin, S. J. Bus, J. M. Sunshine, and T. H. Burbine, Muses-C Target Asteroid 1998 SF36: A Reddened Ordinary Chondrite, *Annual Meteoritical Society Meeting*, **64**, 5032, 2001.

Bowell, E., B. Hapke, D. Domingue, K. Lumme, J. Peltoniemi, and A. W. Harris, Application of photometric models to asteroids, in *Asteroids II*, edited by R. P. Binzel, T. Gehrels, and M. S. Matthews, 525–556, University of Arizona Press, Tucson, AZ, 1989.

Bowen, I. and J. A. Vaughan, Optical design of the 40-in telescope and of the Irenee DuPont telescope at Las Campanas Observatory, Chile, *Applied Optics*, **12**, 1430–1435, 1973.

Demura, H., S. Kobayashi, E. Nemoto, N. Matsumoto, M. Furuya, A. Yukishita, N. Muranaka, H. Morita, K. Shirakawa, M. Maruya, H. Ohyama, M. Uo, T. Kubota, T. Hashimoto, J. Kawaguchi, A. Fujiwara, J. Saito, S. Sasaki, H. Miyamoto, and N. Hirata, Pole and Global Shape of 251453 Itokawa, *Science*, **312**, 1347–1349, 2006.

Dermawan, B., T. Nakamura, H. Fukushima, H. Sato, F. Yoshida, and Y. Sato, CCD Photometry of the Muses-C Mission Target: Asteroid (25143) 1998 SF36, *PASJ*, **54**, 635–640, 2002.

Dressler, A., T. Hare, B. C. Bigelow, and D. J. Osip, IMACS: the wide-field imaging spectrograph on Magellan-Baade, *Proc. SPIE Ground-based and Airborne Instrumentation for Astronomy*, **6269**, 0F, 2006.

Giorgini, J. D., D. K. Yeomans, A. B. Chamberlin, P. W. Chodas, R. A. Jacobson, M. S. Keesey, J. H. Lieske, S. J. Ostro, E. M. Standish, and R. N. Wimberly, JPL's On-Line Solar System Data Service, *Bulletin of the American Astronomical Society*, **28**(3), 1158, 1996.

Gutiérrez, P. J., B. J. R. Davidsson, J. L. Ortiz, R. Rodrigo, and M. J. Vidal-Nuez, Comments on the amplitude-phase relationship of asteroid lightcurves: Effects of topography, surface scattering properties, and obliquity, *Astronomy & Astrophysics*, **454**, 367–377, 2006.

Howell, E., Probing asteroid composition using visible and near-infrared spectroscopy, Ph.D. thesis, Univ. Arizona, 1995.

Ishiguro, M., M. Abe, Y. Ohba, A. Fujiwara, T. Fuse, H. Terada, M. Goto, N. Kobayashi, A. T. Tokunaga, and S. Hasegawa, Near-Infrared Observations of MUSES-C Mission Target, *Publications of the Astronomical Society of Japan*, **55**, 691–699, 2003.

Kaasalainen, M., T. Kwiatkowski, M. Abe, J. Piironen, T. Nakamura, Y. Ohba, B. Dermawan, T. Farnham, F. Colas, S. Lowry, P. Weissman, R. J. Whitely, D. J. Tholen, S. M. Larson, M. Yoshikawa, I. Toth, and F. P. Velichko, CCD photometry and model of MUSES-C target 25143 Itokawa, *Astronomy & Astrophysics*, **405**, L29–L32, 2003.

Kaasalainen, M., personal communication, 2004.

Landolt, A. U., UBVRI photometric standard stars in the magnitude range 11.5–16.0 around the celestial equator, *Astronomical Journal*, **104**, 340–371, 1992.

Landsman, W. B., The IDL Astronomy User's Library, in *Astronomical Data Analysis Software and Systems II, A.S.P. Conference Series*, edited by R. J. Hanisch, R. J. V. Brissenden, and J. Barnes, **52**, 246, 1993.

Lang, K., *Astrophysical Formulae 2*, Springer-Verlag, New York, 1992.

Lederer, S. M., D. Domingue, F. Vilas, M. Abe, T. L. Farnham, K. S. Jarvis, S. C. Lowry, Y. Ohba, P. R. Weissman, L. M. French, H. Fukai, S. Hasegawa, M. Ishiguro, S. M. Larson, and Y. Takagi, Physical characteristics of Hayabus target Asteroid 25143 Itokawa, *Icarus*, **173**, 153–165, 2005.

Lederer, S. M., D. L. Domingue, J. E. Thomas-Osip, F. Vilas, D. J. Osip, S. L. Leeds, and K. S. Jarvis, The 2004 Las Campanas/Lowell Observatory campaign II. Surface properties of Hayabusa target Asteroid 25143 Itokawa inferred from Hapke modeling, *Earth Planets Space*, **60**, this issue, 49–59, 2008.

Lowry, S. C., P. R. Weissman, M. D. Hicks, R. J. Whiteley, and S. Larson, Physical properties of Asteroid (25143) Itokawa, *Icarus*, **176**, 408–417, 2005.

Müller, T. G., T. Sekiguchi, M. Kaasalainen, M. Abe, and S. Hasegawa, Thermal infrared observations of the Hayabusa spacecraft target asteroid 25143 Itokawa, *Astronomy & Astrophysics*, **443**, 347–355, 2005.

Osip, D. J., M. M. Phillips, R. Bernstein, G. Burley, A. Dressler, J. L. Elliot, E. Persson, S. A. Shectman, and I. Thompson, First-generation instruments for the Magellan telescopes: characteristics, operation, and performance, *Proc. SPIE Ground-based Instrumentation for Astronomy*, **5492**, 49–59, 2004.

Ostro, S. J., L. A. M. Benner, M. C. Nolan, C. Magri, J. D. Giorgini, D. J. Scheeres, S. B. Broschart, M. Kaasalainen, D. Vokrouhlicky, S. R. Chesley, J.-L. Margot, R. F. Jurgens, R. Rose, D. K. Yeomans, S. Suzuki, and E. M. de Jong, Radar observations of Asteroid 25143 (Itokawa), *Meteoritics & Planetary Science*, **39**, 407–424, 2004.

Persson, S. E., D. C. Murphy, W. Krzeminski, M. Roth, and M. J. Reike, A New System of Faint Near-Infrared Standard Stars, *Astronomical Journal*, **116**, 2475–2488, 1998.

Persson, S. E., D. C. Murphy, S. M. Gunnels, C. Birk, A. Bagish, and E. Koch, The Las Campanas Infrared Survey Camera, *Astronomical Journal*, **124**, 619–634, 2002.

Saito, J., H. Miyamoto, R. Nakamura, M. Ishiguro, T. Michikami, A. M. Nakamura, H. Demura, S. Sasaki, N. Hirata, C. Honda, A. Yamamoto, Y. Yokota, T. Fuse, F. Yoshida, D. J. Tholen, R. W. Gaskell, T. Hashimoto, T. Kubota, Y. Higuchi, T. Nakamura, P. Smith, K. Hiraoka, T. Honda, S. Kobayashi, M. Furuya, N. Matsumoto, E. Nemoto, A. Yukishita, K. Kitazato, B. Dermawan, A. Sogame, J. Terazono, C. Shinohara, and H. Akiyama, Detailed Images of Asteroid 25143 Itokawa from Hayabusa, *Science*, **312**, 1341–1344, 2006.

Sykes, M. V., R. M. Cutri, J. W. Fowler, D. J. Tholen, M. F. Skrutskie, S. Price, and E. F. Tedesco, The 2MASS Asteroid and Comet Survey, *Icarus*, **146**, 161–175, 2000.

Tody, D., The IRAF data reduction and analysis system, in *Proc. SPIE Instrumentation in Astronomy VI*, edited by D.L. Crawford, **627**, 733–748, 1986.

Tody, D., IRAF in the nineties, in *Astronomical Data Analysis Software and Systems II, A.S.P. Conference Series*, edited by R. J. Hanisch, R. J. V. Brissenden, and J. Barnes, **52**, 173–183, 1993.

Tokunaga, A. T., Infrared Astronomy, in *Allen's Astrophysical Quantities Fourth Edition*, edited by A. N. Cox, 143–168, Springer, New York, 2001.

Tomasko, M. G., Photometry and polarimetry of Jupiter, in *Jupiter*, edited by T. Gehrels, 486–515, University of Arizona Press, Tucson, 1976.

Zappalà, V., A. Cellino, A. M. Barucci, M. Fulchignoni, and D. F. Lupishko, An analysis of the amplitude-phase relationship among asteroids, *Astronomy & Astrophysics*, **231**, 548–560, 1990.

J. E. Thomas-Osip (e-mail: jet@lco.cl), S. M. Lederer, D. J. Osip, F. Vilas, D. Domingue, K. Jarvis, and S. L. Leeds